

Estimation of thermal shock resistance of fine porous alumina by infrared radiation heating method

Sawao HONDA,[†] Yuuki OGIHARA, Tsunego KISHI,* Shinobu HASHIMOTO** and Yuji IWAMOTO

Department of Frontier Materials, Graduate School of Engineering, Nagoya Institute of Technology, Gokiso-cho, Showa-ku, Nagoya, Aichi 466-8555

*Department of Environmental and Materials Engineering, Nagoya Institute of Technology, Gokiso-cho, Showa-ku, Nagoya, Aichi 466-8555

**Department of Materials Science and Engineering, Graduate School of Engineering, Nagoya Institute of Technology, Gokiso-cho, Showa-ku, Nagoya, Aichi 466-8555

The thermal shock resistance of α -alumina porous capillary, the support material for hydrogen-permselective microporous ceramic membrane was studied. To study the effect of porosity on the thermal shock resistance systematically, porous alumina with different porosities was fabricated, and the thermal shock resistance of the fabricated samples as well as the porous capillary was estimated by the infrared radiation heating method. The mechanical and thermal properties concerned to the thermal shock resistance were also measured and the effect of the porosity on the properties was carefully examined. The fracture strength was not changed with temperature, but decreased with the porosity. The fracture toughness, Young's modulus and thermal conductivity were also decreased with porosity. Thermal shock resistance of porous alumina was estimated quantitatively by the experimental thermal shock parameters, thermal shock strength, R_{1c} and thermal shock fracture toughness, R_{2c} . The thermal shock parameters of porous alumina were much lower than dense alumina, and decreased with porosity due to the decreasing of fracture strength and thermal conductivity. The experimental thermal shock strength was good accordance with that calculated from the material properties in this study. Thermal shock strength of porous alumina capillary at service temperature could be estimated by the comparison experimental and calculated thermal shock strength.

©2009 The Ceramic Society of Japan. All rights reserved.

Key-words : Thermal shock resistance, Mechanical properties dependence, Thermal properties, Infrared radiation heating, Porous alumina

[Received August 18, 2009; Accepted October 15, 2009]

1. Introduction

Porous ceramics has been used for environmental and energy industries. In hydrogen (H_2) production process, for example methane (CH_4) steam reforming reaction, H_2 gas can be produced at approximately 1073 K, and must be separated from other mixed gas using palladium-based membranes or microporous ceramic membranes. Microporous ceramic membranes have relatively high gas permeability and good stability at high temperature. Porous alumina capillary has been investigated as support material for the ceramic membranes.¹⁾ Generally, the porous capillary support has fine pores (about 0.1 μm) and relatively large porosity (above 40%). This porous structure design is essential for the gas separation membrane support to minimize the pressure drop of the permeating gas.

However, thermal shock fracture will be occurred by the thermal stress which is caused by a rapid temperature change realized to the reaction temperature, or unexpected emergency stop of the H_2 production reactor. The estimation of thermal shock resistance is important to the application of porous alumina capillary to ceramic membrane for the H_2 production process.

In past studies, many researches of the mechanical and thermal properties of porous ceramics have been reported. The limited literatures, however, exist on the estimation of the thermal

shock resistance properties for the porous ceramics, especially high porosity ceramics.²⁾⁻⁴⁾ The quantitative estimation of the relation thermal shock resistance and porous structure is insufficient.

The water quenching mainly has been used for the estimation of thermal shock resistance. In the case of application to the porous ceramics, however, the penetration of quenching medium through the pores and instability of heat transfer coefficient at the rough surface were afraid to cause difficulty in the accurate estimation. On the other hand, we have been evaluated thermal shock resistance of the dense ceramics by the infrared radiation heating (IRH) method.⁵⁾⁻⁸⁾ It has advantage that can be stable heat flux condition and quantitative estimation of thermal shock resistance using thermal shock parameters.

In this study, we investigate to apply the IRH method to the high porosity ceramics as thermal shock testing method. Porous alumina with fine pore size and different porosities are fabricated by change of the sintering temperature. Thermal shock resistance is estimated by the IRH method, and the mechanical and thermal properties concerned to the thermal shock resistance are also measured. The relations between these properties and porosity are evaluated by thermal shock parameters, and the thermal shock resistance of porous alumina capillary is estimated quantitatively.

[†] Corresponding author: S. Honda; E-mail: honda@nitech.ac.jp

2. Experimental procedure

2.1 Porous alumina preparation

The specimen sizes used in this study are listed in **Table 1**. Preparation of porous alumina capillary specimen (CS) was reported by KOJIMA, et al.¹⁾ Because of the shape and size of the capillary was not suitable for the specimen of thermal shock resistance and some other properties, bulk specimen was fabricated by the powder forming process in this study (PS). The green tubes consisted of α -alumina powder (Taimei Chemicals Co., Ltd., TM-DA, 0.3 μm in mean particle size) and polymer binder was prepared by a dry-wet spinning method, which was grinded using the mortar. After this grinded powder was passed through a 60 mesh sieve, it was pressed by uniaxially load (0.4 MPa) using disk shaped dies with the diameter 20 or 50 mm. These green disks were sintered by partial sintering method in the temperature at 1423 (PS14), 1523 (PS15) and 1623 (PS16) K for 30 min in air. By changing the sintering temperature, the porosity of the porous alumina was controlled. Another porous alumina specimen with different pore size was prepared by sheet forming process (SS) using same grinded powder, sintered at 1423 K. All of the sintered bodies were cutting with diamond saw to the various specimen sizes.

2.2 Mechanical and thermal properties

The density and porosity of the porous alumina were measured by the Archimedes method. The mean pore diameter was determined by a mercury porosimeter (Shimadzu Co., PORE SIZER 9320). The total porosity of the porous alumina was calculated as:

$$P_t = P_{op} + (1 - P_{op}) \left(1 - \frac{\rho_a}{\rho} \right) \quad (1)$$

where P_t is total porosity, P_{op} open pore porosity, ρ_a apparent density, and ρ theoretical density. The fracture strength, fracture toughness, and Young's modulus were evaluated by a universal testing machine with electric furnace (Instron Co., 5582) at a cross head speed of 1.0 mm/min. The fracture strength of CS, σ_c , was calculated as:

$$\sigma_c = \frac{8D_2LP_t}{\pi(D_2^4 - D_1^4)} \quad (2)$$

where P_f is fracture load, D_2 outer diameter, D_1 inner diameter, and L lower span. On the other hand, the fracture strength test of PS was based on JIS R 1601. Fracture toughness was estimated by the Single edge V-notched beam (SEVNB) method.⁹⁾ The specimens similar to those for bending test in dimensions were introduced at the lower surface with a sharp V-notch. The radius of curvature at the V-notch tip was about 20 μm . The fracture toughness, K_{IC} , test was based on JIS R 1607, and it was calculated as:

$$K_{IC} = \frac{3}{2} \frac{P_f L}{BV^{3/2}} Y \sqrt{\xi} \quad \xi = \frac{\gamma}{V} \quad (3)$$

$$Y = \frac{1.99 - \xi(1 - \xi)(2.15 - 3.93\xi + 2.7\xi^2)}{(1 + 2\xi)(1 - \xi)^{3/2}} \quad (\text{at } L/T = 4.0)$$

where B is thickness of specimen, V width of specimen, Y shape factor, and γ notch length. Young's modulus was estimated by the slope of the stress-strain curve on the compression testing. Strain was measured by the strain gage attached to a normal surface to the compression surface. Thermal conductivity was measured by the laser flash thermal constants analyzer (Ulvac-Riko Inc., TC-7000) based on JIS R 1611, and the coefficient of thermal expansion was determined with a differential thermal expansion meter (Shimadzu Co., TMA-50) based on JIS R 1618. The temperature dependences of these thermal properties were also studied by changing the measured temperatures, from R.T. to 1023 K. All of the values in properties of dense alumina ($P = 0$), σ_0 , E_0 , K_0 and λ_s were used for the values of previous work.⁷⁾

2.3 Thermal shock test by Infrared radiation heating

Disk-shaped specimens were prepared for the thermal shock strength, R_{1c} test, and a V-notch (notch length $c = 2.0$ mm) was produced on the disk edge for the thermal shock fracture toughness, R_{2c} test, as showed in **Fig. 1**. Two thermocouples were attached symmetrically to the disk surface at 10 mm from the center of the disk, to provide for estimation of the heating efficiency and the temperature at the fracture point. Graphite was coated onto the heating areas ($2a = 14.5$ mm) on both sides of the disk to enhance absorptivity of the infrared rays. The apparatus used for the IRH method was represented in **Fig. 2**. The

Table 1. Experimental Conditions and Specimen Sizes in the Measured Properties

Property	Sample name	Method	Temperature (K)	Specimen shape	Specimen size (mm)
Fracture strength	CS	Three-point bending (Lower span 30 mm)	R.T., 873, 10232	Capillary	2.8 × 2.5 × 40 (outer × inner × length)
	PS	Three-point bending (Lower span 8 mm)	R.T.	Rectangular Bar	2 × 2 × 10
Fracture toughness	PS	SEVNB (Lower span 8 mm)	R.T.	Rectangular Bar	2 × 2 × 10 (Notch length 1.0)
Young's modulus	PS	Compression test with strain-gage	R.T.	Rectangular Bar	5 × 5 × 10
Thermal conductivity	PS	Laser flash	R.T., 473, 673 873, 1023	Disk	φ10 × 1
Thermal expansion coefficient	PS	Differential thermal expansion meter	R.T., 473, 673 873, 1023	Rectangular Bar	5 × 5 × 10
Thermal shock resistance	PS, SS	Infrared radiation heating	R.T. (Initial temp.)	Disk	φ37-40 (2r ₀) × 1.1 (H) (c = 2.0)

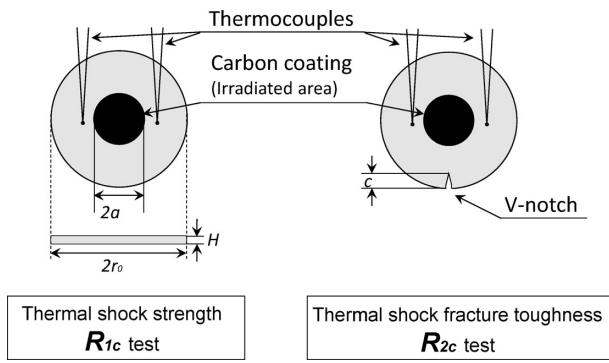


Fig. 1. Schematic diagram of disk specimens in infrared radiation heating method.

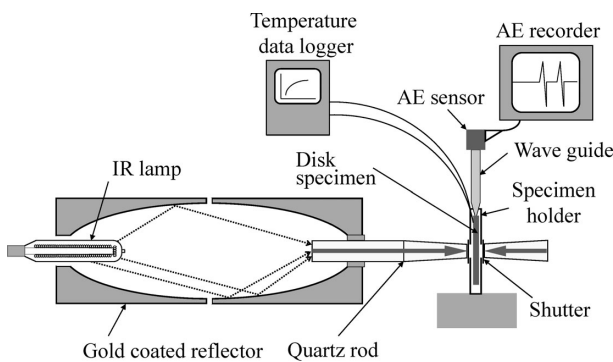


Fig. 2. Schematic diagram of thermal shock test by infrared radiation heating method.

surface of the specimen disk was covered with heat insulating material, to prevent infrared radiation except in the heating area and heat loss by air convection around the specimen. The infrared rays were radiated from the two lamps at both sides of the specimen, through the ellipsoid mirror and quartz bars. After the supplied electric powers to the lamps were obtained to setting values, the center of the disk was irradiated by opening an aluminum shutter. The thermal shock fracture was occurred by the thermal stress generated from temperature difference between the center and circumference of the disk. Start time of crack propagations was determined with an acoustic emission (AE) device through the wave guide. The maximum tensile thermal stress and stress intensity factor at the V-notch tip in specimen were calculated numerically at the failure time, t , determined by AE signals.

2.4 Thermal shock parameters

Several thermal shock resistance parameters were suggested in the past studies.^{10,11)} For standardized thermal shock testing, however, thermal shock resistance parameters as material constants should be established on the basis of the physical properties of materials. We proposed two thermal shock parameters as physical properties: thermal shock strength, representing the resistance to thermal shock fracture, and thermal shock fracture toughness, denoting the resistance to the initiation of crack propagation.¹²⁾ A theory of the thermal shock parameters is described below.

When considering the thermal stress problem of a hot plate subjected to rapid cooling, the relation between the temperature difference, $\Delta\theta$, and the maximum stress occurring in the plate,

σ_{\max} , for a relatively small Biot number is expressed by the following approximation:¹³⁾

$$\Delta\theta = \frac{\lambda\sigma_{\max}}{E\alpha} \frac{3.25(1-\nu)}{hl} \quad (4)$$

where E is the Young's modulus, α the thermal expansion coefficient, ν the Poisson ratio, λ the thermal conductivity, h the heat transfer coefficient, and l the half-thickness of the plate. Excluding the numerical constant and the factors related to experimental environment h , l and $1-\nu$ from Eq.(4), the critical value of the combination of the material properties is defined as follows:

$$R_{1c} = \frac{\lambda\sigma_f}{E\alpha} \quad [\text{W}\cdot\text{m}^{-1}] \quad (5)$$

where σ_f is the modified strength estimated from fracture strength of the material with volume effect calculation.

For a plate with a mode I crack under cooling, the stress intensity factor is expressed by

$$K_I = Z\sigma_{\max}\sqrt{\pi c} \quad (6)$$

where Z is the shape factor and c the half-crack length. By substituting Eq.(6) into Eq.(4), the following equation is obtained:

$$\Delta\theta = \frac{\lambda K_I}{E\alpha} \frac{3.25(1-\nu)}{hlZ\sqrt{\pi c}} \quad (7)$$

Excluding the numerical constant and the factors related to the experimental environment from Eq.(7), the critical value of the combination of the material properties defined as

$$R_{2c} = \frac{\lambda K_{IC}}{E\alpha} \quad [\text{W}\cdot\text{m}^{-0.5}] \quad (8)$$

where K_{IC} is the fracture toughness of the material. Eqs.(5) and (8), which are defined combinations of the material properties, are referred to herein as 'calculated values' of the thermal shock parameters.

The thermal shock parameters can be evaluated directly from the electrical charge and the testing conditions of the IR heating technique. The heat flux, q , in the specimen is calculated from the electric charge as

$$q = \frac{\eta\omega}{\pi a^2} \quad (9)$$

where η is the efficiency of the transforming electric power into heat flux, ω the supplied electronic power to the IR ramps, and a the radius of the heated area on the disk.

The maximum circumferential component of the thermal stress in the disk, $\sigma_{\theta\max}$, is defined in the following nondimensional form:

$$S_{\max} = \frac{\sigma_{\theta\max}}{E\alpha Q} \quad (10)$$

where Q is a variable having the dimension of temperature defined as

$$Q = \frac{qn_0^2}{H\lambda_i} \quad (11)$$

where H is the thickness of the disk, r_0 the radius of the disk, and λ_i the thermal conductivity of the material at the initial temperature. Also, the nondimensional stress intensity factor, N_I , is defined as follows.

$$N_1 = \frac{K_I}{E\alpha Q\sqrt{\pi c}} \quad (12)$$

In the specimen of the R_{2c} test, K_I and c correspond to the stress intensity factor at the V-notch tip and c the V-notch length, respectively. Substituting Eq.(10) and Eq.(12) into Eq.(5) and Eq.(8), respectively, we got

$$R_{1c} = S \frac{\eta\omega}{\pi H (a/r_0)^2} \quad [\text{W}\cdot\text{m}^{-1}] \quad (13)$$

$$R_{2c} = N_1 \sqrt{\pi c} \frac{\eta\omega}{\pi H (a/r_0)^2} \quad [\text{W}\cdot\text{m}^{-0.5}] \quad (14)$$

Equations (13) and (14), defined combinations of the experimental conditions, are referred to herein as ‘experimental values’ of the thermal shock parameters. The changes with time of S and N_1 are calculated from the transient temperature distribution of the disk specimen using the data of thermocouple. The critical values of S and N_1 are those of at the fracture time, t . The calculated and experimental values of thermal shock parameters on the dense ceramics were in good agreement for the thermal shock test using the IRH.^(6,7)

3. Results and discussion

3.1 Properties of porous alumina

Figure 3 shows total porosity and mean pore size (d) of sintered porous alumina. The porosity of PS decreased with an increasing sintering temperature. The mean pore sizes, however, were almost same among PS series. The sintered porous alumina capillaries, which were fabricated by the dry-wet spinning method, also showed the different porosity with same pore diameter of approximately $0.1 \mu\text{m}$ by changing sintering temperature.¹⁾ The effect of the porosity on the properties of porous alumina could be evaluated by the comparison of PS series. On the other hand, as the porosity of CS, SS, and PS15 were almost same, the effect of pore size could be estimated. **Figure 4** shows a typical SEM image of the as-sintered surface in PS14. The alumina grain and their necking did not grow at this sintering temperature.

Figure 5 shows the temperature dependence of the three-point bending strength, σ_c , in CS. The mean strength of σ_c was slightly decreased with an increasing temperature. The fracture

strength at 1073 K was decreased about 7% compared to that of room temperature. The Weibull analysis for the fracture strength at room temperature was carried out. The Weibull modulus ($m = 15.2$) of the CS agreed with the results of porous alumina tube in other research.^{1),14)} A scatter of fracture strength seemed to be increased with increasing temperature. Nishikawa et al.¹⁵⁾ reported that the fracture strength of 1073 K was decreased about 10% compared to that of room temperature in porous alumina (porosity of 40%, pore size of $1.5\text{--}10 \mu\text{m}$). This result showed that the effect of the mean pore size on the temperature dependency of fracture strength was not so large.

Figure 6 shows the relation of the porosity and three-point bending strength in PS, σ_p , and σ_c at room temperature. The values of σ_p were decreased with an increasing porosity. The σ_c was agreed with the relation between σ_p and porosity. Many researches have reported to represent the relationship between porosity (P) and fracture strength (σ). The following general equation was proposed by Ryshkewitch¹⁶⁾ and Knudsen.¹⁷⁾

$$\sigma = \sigma_0 \exp(-bP) \quad (15)$$

where σ_0 is fracture strength at $P = 0$, and b an empirical constant estimated from slope of semi log plot. The b value of PS (5.2) was agreed with that of the other research in porous alumina (5.1).¹⁸⁾ Eudier suggested the following equation by a model of

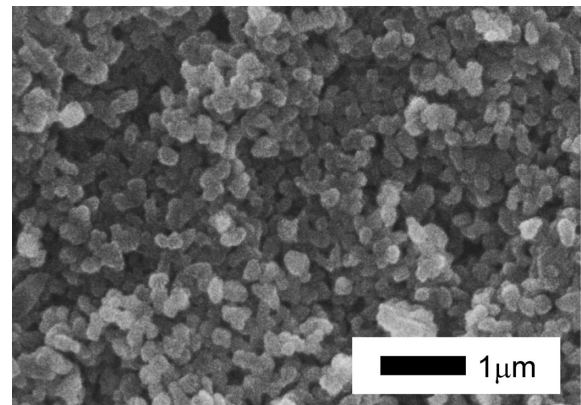


Fig. 4. SEM image of the as-sintered surface in porous alumina of PS14.

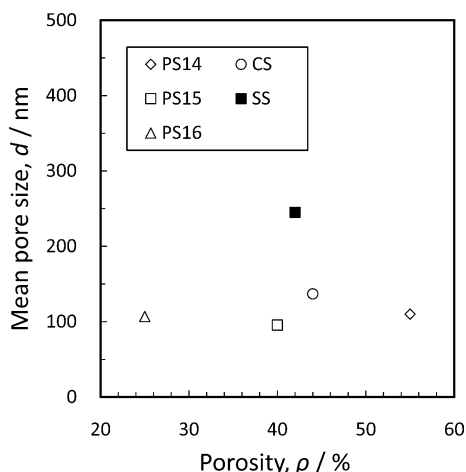


Fig. 3. Porosity and mean pore sizes of tested porous alumina.

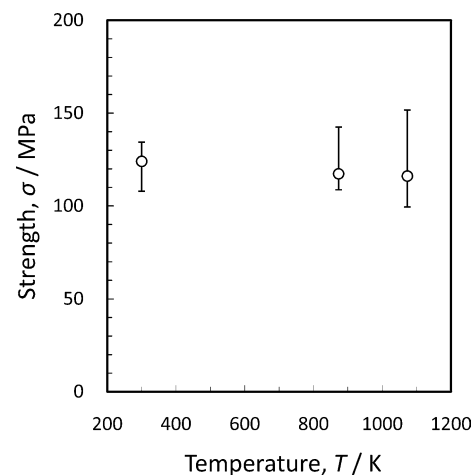


Fig. 5. Temperature dependence of fracture strength in CS.

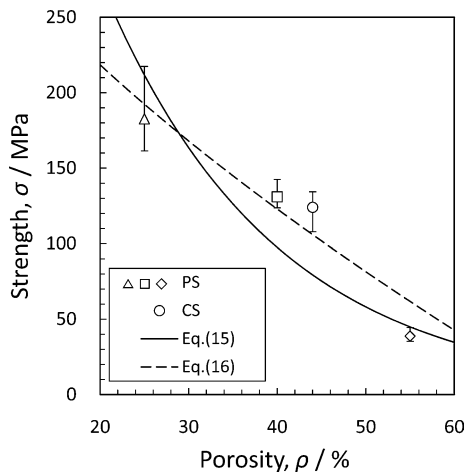


Fig. 6. Porosity dependence of fracture strength in PS, and comparison with CS.

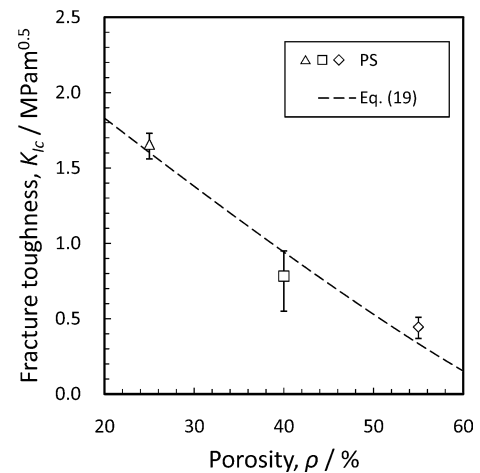


Fig. 8. Porosity dependence of fracture toughness in PS.

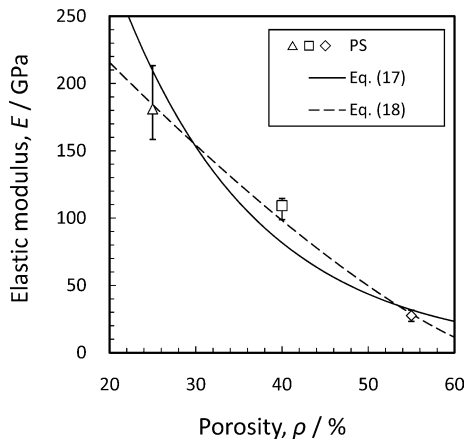


Fig. 7. Porosity dependence of Young's modulus in PS.

minimum cross section area of matrix.¹⁹⁾

$$\sigma = \sigma_0 (1 - KP^{2/3}) \tag{16}$$

where $K = \pi (3/4\pi)^{2/3}$. As compared the two equations, it was seemed to fit the Eq.(16). The other research of fracture strength in porous alumina with sub-micron pore size fabricated by the partial sintering method was agreed with the Eq.(16).²⁰⁾

Figure 7 shows the relation of the porosity and Young's modulus, E , in PS at room temperature. The E , were decreased with an increasing porosity as well as fracture strength. The E value of PS were agreed with porous alumina having sub-micron²⁰⁾⁻²²⁾ or micron pore size^{20),23)} in the same porosity. Young's modulus was slightly depended on the pore size.^{20),23)} Many equations had been reported to represent the relationship between porosity (P) and Young's modulus (E). The following equation was proposed by Spprigs²⁴⁾ and Knudsen:²⁵⁾

$$E = E_0 \exp(-bP) \tag{17}$$

where E_0 is Young's modulus at $P = 0$, and b an empirical constant. The b value of PS calculated from eq. was 6.3. As compared with other porous alumina with the sub-micron (6.5)²⁰⁾ and micron (4.0–4.3,²⁰⁾ 4.0²⁵⁾ pore size, the b values of porous alumina with sub-micron pore size were higher than that of micron pore size. This results were attributed to lower E of porous

alumina with sub-micron pore size in high porosity regions. Because the sub-micron porous alumina was sintered at lower sintering temperature, lower Young's modulus was appeared by insufficient neck growth of alumina grains,²⁰⁾ as showed in Fig. 4. The following equation was suggested for the Young's modulus of partial sintering porous alumina.^{21),22)}

$$E = E_0 \left(1 - \frac{P}{P_0}\right)^n \tag{18}$$

where E_0 is Young's modulus at $P = 0$, P_0 a porosity of the green bodies of the specimen (about 65% in PS), and n an empirical constant. The n value of PS (1.38) was similar to the other study (1.35).²¹⁾

Figure 8 shows the relation of the porosity and fracture toughness, K_{Ic} , in PS at room temperature. The K_{Ic} , were decreased with an increasing porosity. The following equation was suggested for the fracture toughness of partial sintering porous alumina as well as Young's modulus.^{21),22)}

$$K = K_0 \left(1 - \frac{P}{P_0}\right)^n \tag{19}$$

where K_0 is fracture toughness at $P = 0$, and n an empirical constant. The n value of PS (1.13) was similar to the other study (1.15).²¹⁾

Figure 9 shows the temperature dependences of thermal conductivity, λ , in PS. The λ were decreased with an increasing temperature as well as dense alumina. They were also decreased with an increasing porosity. Many equations have been reported to represent the relationship between porosity (P) and thermal conductivity (λ). The following equation was proposed by Russel.²⁶⁾

$$\lambda = \lambda_s \frac{P^{2/3} + \kappa(1 - P^{2/3})}{P^{2/3} - P + \kappa(1 - P^{2/3} + P)} \quad \kappa = \frac{\lambda_s}{\lambda_f} \tag{20}$$

where λ_s is thermal conductivity of solid part (dense alumina matrix), λ_f thermal conductivity of fluid part (air). Though the calculated values with solid lines were compared with experimental plot in Fig. 9, these values were not agreed with the experimental values. The λ in this study was apparently lower than the values estimated by these equations and the other research.^{26),27)} Because of the densification of alumina matrix was not progressed with lower sintering temperature, as showed

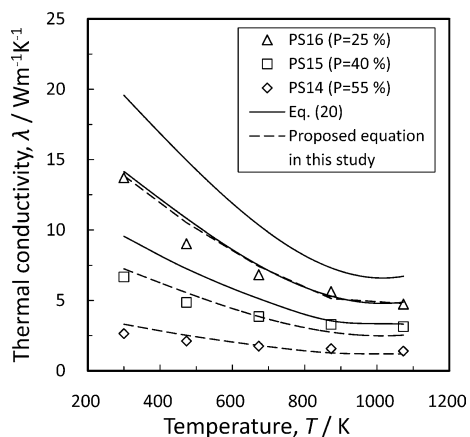


Fig. 9. Temperature dependence of thermal conductivity in PS.

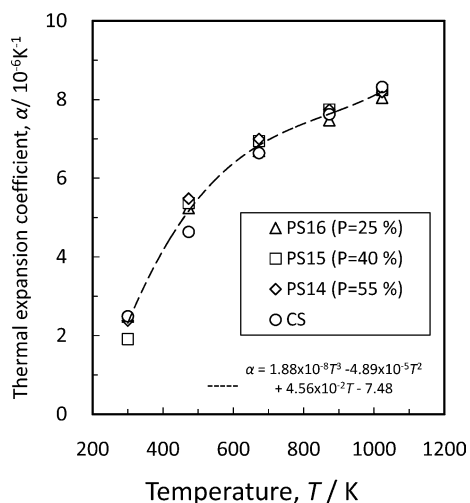


Fig. 10. Temperature dependence of thermal expansion coefficient in PS, and comparison with CS.

in Fig. 4, thermal conductivity of solid part of porous alumina in this study was lower than that of the dense alumina. Therefore, we thought that λ_s was also depended on the porosity, and tried to calculate λ by substituting λ_s the dense alumina by the value calculated by Eq.(20). These modified values with broken lines were agreed approximately with the experimental values.

Figure 10 shows the temperature dependences of thermal expansion coefficient, α , in PS. The α were decreased with an increasing temperature as well as dense alumina. They were not changed with porosity different from the other properties. In literature, alumina refractories with porosity 0.3 and 0.7 showed the same thermal expansion coefficient.²⁸⁾ This result suggests that the thermal expansion of porous alumina is not affected by the porous characteristics such as porosity. Temperature dependence of α could be well fitted by a cubic equation.

3.2 Thermal shock test of porous alumina

A photograph of the porous alumina (PS) specimen after the thermal shock strength test was showed in Fig. 11. A fracture was occurred at 2–3 mm inside the edge of the specimen disk (indicated by arrow). After the crack propagation to a straight line toward the center of the disk, it was branching and curved. This pattern of the crack propagation was also observed in the

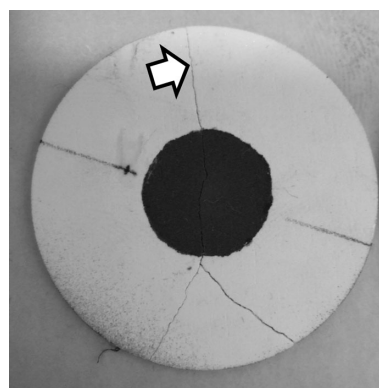


Fig. 11. Photograph of fractured specimen after thermal shock strength test.

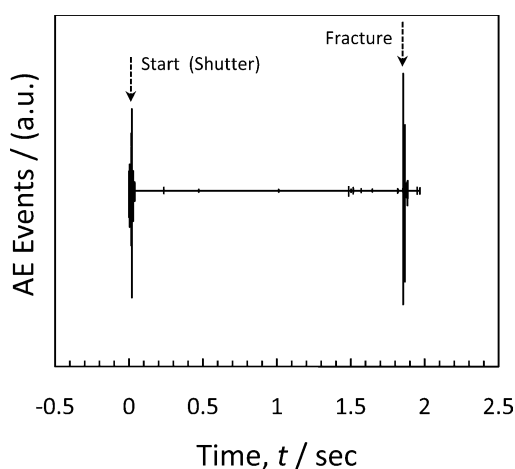


Fig. 12. AE signal of thermal shock test.

thermal shock test using IRH technique for dense ceramics.⁶⁾ In the specimen of the higher porosity above 40%, the crack was propagated in a straight line toward the edge in the opposite side of the disk without branching.

The AE signal detected during the thermal shock test was shown in Fig. 12. The start time of heating was decided by the sound of a shutter. In this test, AE signal of the thermal shock fracture was clearly detected after 1.85 sec from the start of heating. Therefore, the fracture time, t was determined to 1.85 in this test. The numbers of AE events were correlated with the number of cracks or the retained strength of specimen after the thermal shock test.^{29),30)} In the IRH method, a number of AE events were not changed in each test because only a few large cracks were propagated, as showed in Fig. 11. In a porous material, the AE was easily attenuated by a scattering in pores. The thermal shock testing method by water quenching, the AE of the thermal shock fracture was difficult to detect by the noise of boiling water. The IRH method was possible to detect AE clearly without the effect of the noise even when the porous ceramics was tested. Knowledge of the fracture time accurately was enabled to analyze of the thermal stress and the quantitative evaluation of thermal shock resistance. The IRH method was proved to be useful for the thermal shock resistance of the porous ceramics.

Figure 13 shows the relation between experimental R_{1c} of PS obtained from Eq.(13), by thermal stress calculation and various experimental conditions, and calculated R_{1c} derived from Eq.(5),

based on measured properties of PS. The R_{1c} decreased with an increasing the porosity. For all the specimens with different porosity, the experimental R_{1c} showed good agreement with the calculated R_{1c} . Thus, the thermal shock strength of porous alumina ceramics could be estimated by their material properties.

Figure 14 shows the relation between experimental R_{2c} of PS obtained from Eq.(14), by calculation of stress intensity factor at the notch and various experimental conditions, and the calculated R_{2c} derived from Eq.(8), based on the measured properties of PS. The experimental R_{2c} showed the larger scatters than R_{1c} in every porosity, and decreased with an increasing the porosity as well as R_{1c} . The experimental R_{2c} was showed not so good agreement with the calculated R_{2c} . In past studies, we reported that the experimental R_{2c} was agreed with calculated R_{2c} on various dense ceramics.^{6),7)} Thus, this disagreement was caused by the porous specimen. The experimental R_{2c} was higher than the calculated R_{2c} in PS15 and PS16. Because of the disagreement was not appeared in R_{1c} , it was thought to be ascribable to over-estimate the critical value of stress intensity factor by the relaxation of the stress intensity at the notch-tip in thermal shock specimen by compare with the K_{1c} measured by the SEVNB method. If the relaxation was caused by existence of pore, lower porosity specimen with higher inhomogeneity of pore distribution showed the higher scatter of stress intensity factor. Furthermore, the specimen thickness of the thermal shock test was thinner than SEVNB specimen. Notch shape was easily deformed in the thin disk, and this deformation enhanced the relaxation of stress intensity. These effects may be avoided by the adjustment thickness of disk specimen.

A porosity dependence of thermal shock parameters was investigated by the calculated values from Eqs(5), (8). The E , σ , K_{1c} , and λ were decreased, and α was not changed with porosity. While the decreasing of E enhanced the thermal shock parameters, the decreasing of σ , K_{1c} , and λ lowered it.

Figure 15 shows the relation between the porosity and the experimental R_{1c} in PS and SS. The SS with lager pore size than PS showed lower R_{1c} than PS15 with similar porosity. The fracture strength of porous alumina was depended on the pore size as following equation:^{23),31)}

$$\sigma_f \propto \frac{1}{\sqrt{d}} \tag{21}$$

Thus, the fracture strength is decreased with an increasing pore size. The thermal shock strength was decreased with increasing pore size. In order to estimate the thermal shock strength of CS, thermal shock strength was expressed as a function of porosity by substituted for Eqs.(16), (18), (20), and fitted equation of α into Eq.(5). This function showed a relatively good agreement with the experimental R_{1c} of PS, and the R_{1c} of CS could be predicted 377 W/m at $P = 0.44$. If the material properties are not changed with pore size excluding the fracture strength, the thermal shock strength was also propositional to $d^{-0.5}$ from Eq.(21). In this case, the R_{1c} of CS could be predicted 336 W/m. The thermal shock parameters of dense alumina were evaluated by IRH method in the previous work.^{6),7)} These values were estimated 3000 W/m of R_{1c} and 50 W/m^{0.5} of R_{2c} . The thermal shock resistance of the porous alumina was much lower than that of the dense alumina.

Figure 16 shows the temperature dependences of calculated R_{1c} in PS. The R_{1c} was decreased with an increasing temperature due to the decreasing of λ and increasing of α with temperature. The hydrogen-permeable membrane was used at 873–1073 K of reaction temperature. The thermal shock strength of is decreased about 70 W/m at 1073 K. It is important that the porous alumina capillary of thermal shock resistance could be

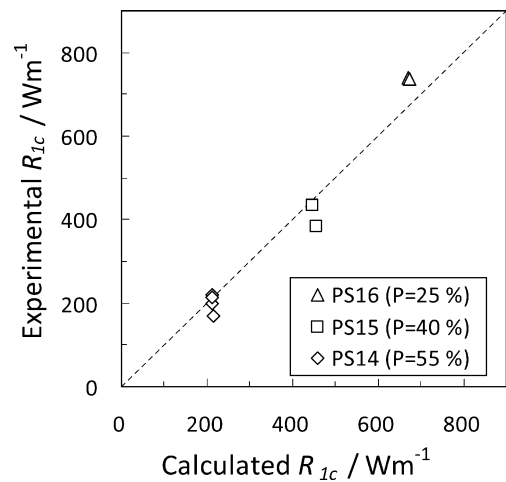


Fig. 13. Comparison of experimental and calculated thermal shock strength in PS.

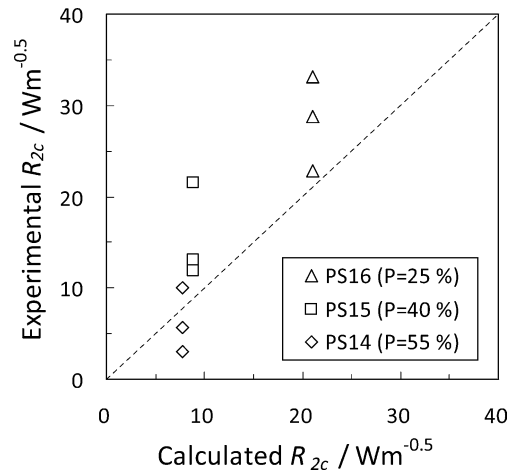


Fig. 14. Comparison of experimental and calculated thermal shock fracture toughness in PS.

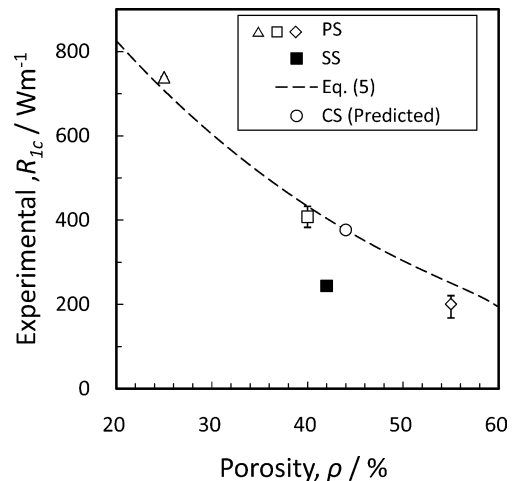


Fig. 15. Porosity dependence of thermal shock strength in PS, and comparison with SS and predicted values of CS.

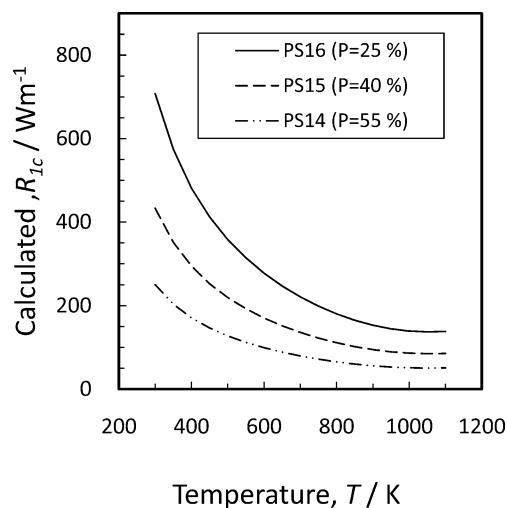


Fig. 16. Temperature dependences of thermal shock strength in PS.

estimated at service temperature.

3. Conclusions

The thermal shock resistance of α -alumina porous capillary was estimated by the infrared radiation heating method. The mechanical and thermal properties concerned to the thermal shock resistance were also measured. The fracture strength was not changed with temperature, but it was decreased with the porosity. The fracture toughness, Young's modulus and thermal conductivity were also decreased with porosity. Thermal expansion coefficient was not changed with porosity. Thermal shock test of porous alumina was executed successfully by the thermal shock fracture and AE signals, and the thermal shock resistance of porous alumina could be estimated quantitatively by the experimental thermal shock parameters. The thermal shock parameters of porous alumina were much lower than dense alumina, and decreased with porosity due to the decreasing of fracture strength, fracture toughness and thermal conductivity. The experimental thermal shock strength was good accordance with the calculated thermal shock strength evaluated by the material properties. Thermal shock strength of porous alumina capillary at service temperature could be estimated by the comparison experimental and calculated thermal shock strength.

Acknowledgement The authors special thank NOK Corporation for providing the raw material powder and capillary samples.

References

- 1) R. Kojima, K. Sato, T. Nagano and Y. Iwamoto, *J. Ceram. Soc. Japan*, **114**, 929–933 (2006).
- 2) R. M. Orenstein and D. J. Green, *J. Am. Ceram. Soc.*, **75**, 1899–1905 (1992).
- 3) V. R. Vedula, D. J. Green and J. R. Hellman, *J. Am. Ceram. Soc.*, **82**, 649–656 (1999).
- 4) J. She, T. Ohji and Z. Y. Deng, *J. Am. Ceram. Soc.*, **85**, 2125–2127 (2002).
- 5) S. Honda, T. Takahashi, S. Morooka, S. Zhang, T. Nishikawa and H. Awaji, *J. Soc. Mat. Sci. Japan*, **46**, 1300–1305 (1997) [in Japanese].
- 6) S. Honda, T. Suzuki, T. Nishikawa, H. Awaji, Y. Akimune and N. Hirosaki, *J. Ceram. Soc. Japan*, **110**, 38–43 (2002) [in Japanese].
- 7) S. Honda, T. Nishikawa, H. Awaji, N. Hirosaki and Y. Akimune, *Ceram. Trans.*, **113**, 127–132 (2002).
- 8) S. Honda, K. Kimata, S. Hashimoto, Y. Iwamoto, M. Yokoyama, J. Shimano, K. Ukai and Y. Mizutani, *Mater. Trans.*, **50**, 1742–1746 (2009).
- 9) H. Awaji and Y. Sakaida, *J. Am. Ceram. Soc.*, **73**, 3522–3523 (1990).
- 10) W. D. Kingery, *J. Am. Ceram. Soc.*, **38**, 3–15 (1955).
- 11) D. P. H. Hasselman, *J. Am. Ceram. Soc.*, **52**, 600–604 (1969).
- 12) H. Awaji, S. Honda and T. Nishikawa, *JSME Int.*, **40**, 414–422 (1997).
- 13) S. S. Manson, NACN TN 2933 (1953).
- 14) S. C. Nanjangud, R. Brezny and D. J. Green, *J. Am. Ceram. Soc.*, **78**, 266–268 (1995).
- 15) T. Nishikawa, Y. Umehara, S. Honda and H. Awaji, *J. Ceram. Soc. Japan, Sup.*, **112**, S1405–S1407 (2004).
- 16) E. Ryshkewitch, *J. Am. Ceram. Soc.*, **36**, 65–68 (1953).
- 17) F. P. Knudsen, *J. Am. Ceram. Soc.*, **42**, 376–387 (1959).
- 18) L. J. Trostel Jr., *J. Am. Ceram. Soc.*, **45**, 563–564 (1962).
- 19) M. Eudier, *Powder Metall.*, **9**, 278–290 (1962).
- 20) T. Nishikawa, A. Nakashima, S. Honda and H. Awaji, *J. Soc. Mat. Sci. Japan*, **50**, 625–629 (2001) [in Japanese].
- 21) T. Ostrowski and J. Rodel, *J. Am. Ceram. Soc.*, **82**, 3080–3086 (1999).
- 22) B. D. Flinn, R. K. Bordia, A. Zimmermann and J. Rodel, *J. Eur. Ceram. Soc.*, **20**, 2561–2568 (2000).
- 23) M. Ashizuka, E. Ishida, T. Matsushita and M. Hisanaga, *J. Ceram. Soc. Japan*, **110**, 554–559 (2002) [in Japanese].
- 24) R. M. Spriggs, *J. Am. Ceram. Soc.*, **44**, 628–629 (1961).
- 25) F. P. Knudsen, *J. Am. Ceram. Soc.*, **45**, 94–95 (1962).
- 26) H. W. Russel, *J. Am. Ceram. Soc.*, **18**, 1–5 (1935).
- 27) Z. Zivcova, E. Gregorova, W. Pabst, D. S. Smith, A. Michot and C. Poulhier, *J. Eur. Ceram. Soc.*, **29**, 347–353 (2009).
- 28) J. B. Austin, *J. Am. Ceram. Soc.*, **35**, 243–253 (1952).
- 29) K. J. Konsztowicz, *J. Am. Ceram. Soc.*, **73**, 502–508 (1990).
- 30) F. Mignard, C. Olagnon and G. Fantozzi, *J. Eur. Ceram. Soc.*, **15**, 651–653 (1995).
- 31) T. Isobe, Y. Kameshima, A. Nakajima, K. Okada and Y. Hotta, *J. Eur. Ceram. Soc.*, **27**, 53–59 (2007).